The Astrophysical Journal, 772:84 (12pp), 2013 August 1 doi:10.1088/0004-637X/772/2/84


# *CHANDRA* VIEW OF THE ULTRA-STEEP SPECTRUM RADIO SOURCE IN A2443: MERGER SHOCK-INDUCED COMPRESSION OF FOSSIL RADIO PLASMA?

T. E. Clarke[1], S. W. Randall[2], C. L. Sarazin[3], E. L. Blanton[4], and S. Giacintucci[5,6]
[1] Naval Research Laboratory, Code 7213, Washington, DC 20375, USA; tracy.clarke.ca@nrl.navy.mil
[2] Harvard Smithsonian Center for Astrophysics, 60 Garden Street, Cambridge, MA 02138, USA
[3] Department of Astronomy, University of Virginia, P.O. Box 400325, Charlottesville, VA 22904-4325, USA
[4] Astronomy Department and Institute for Astrophysical Research, Boston University, Boston, MA 02215, USA
[5] Department of Astronomy, University of Maryland, College Park, MD 20742-2421, USA
[6] Joint Space-Science Institute, University of Maryland, College Park, MD 20742-2421, USA
*Received 2013 April 5; accepted 2013 June 14; published 2013 July 9*

## ABSTRACT

We present a new *Chandra* X-ray observation of the intracluster medium in the galaxy cluster A2443, hosting an ultra-steep spectrum radio source. The data reveal that the intracluster medium is highly disturbed. The thermal gas in the core is elongated along a northwest to southeast axis and there is a cool tail to the north. We also detect two X-ray surface brightness edges near the cluster core. The edges appear to be consistent with an inner cold front to the northeast of the core and an outer shock front to the southeast of the core. The southeastern edge is coincident with the location of the radio relic as expected for shock (re)acceleration or adiabatic compression of fossil relativistic electrons.

*Key words:* galaxies: clusters: general – galaxies: clusters: individual (A2443) – radio continuum: galaxies – X-rays: galaxies: clusters

*Online-only material:* color figures

## 1. INTRODUCTION

Structure formation is thought to occur in a hierarchical manner with objects forming through the gravitational collapse of initial density enhancements and subsequent growth through accretion and merging. The largest gravitationally bound objects in the universe, galaxy clusters, are thought to evolve through multiple mergers, which occur at the intersection of large-scale structure filaments. A typical major cluster merger involves collisions at velocities $\gtrsim$2000 km s$^{-1}$ and can release a total kinetic energy $10^{63-64}$ erg (Sarazin 2000). These mergers are the most energetic events in the universe since the big bang and can drive strong shocks into the intracluster medium (ICM). To date, shocks have been clearly identified in only a small number of merging systems (e.g., Bullet, Markevitch et al. 2002; A520, Markevitch et al. 2005; A2146, Russell et al. 2010; A3667, Finoguenov et al. 2010; A754, Macario et al. 2011; A2744, Owers et al. 2011; MACS0744.8+3927, Korngut et al. 2011; RXCJ1314.4-2515, Mazzotta et al. 2011; A521, Bourdin et al. 2013). The shock energy is dissipated through compression of magnetic fields, particle acceleration or reacceleration, and heating of the ICM. In the presence of magnetic fields, the accelerated relativistic particles can be observable in the radio regime as diffuse synchrotron emission, although the efficiency of shock acceleration is very uncertain (e.g., Kang et al. 2012).

A growing number of clusters of galaxies are known to host regions of extended radio synchrotron emission which have no optical counterparts. These radio sources have low surface brightness, large sizes ($\gtrsim$500 kpc) and steep spectra (see review by Ferrari et al. 2008). They have been observationally classified broadly as halos and relics. Giant radio halos (called radio halos hereafter) are located at cluster centers, show rather regular structure and little or no polarized emission. Relics are seen in projection near the cluster peripheries; they are generally elongated in shape and are often highly polarized. Roughly 80 clusters have been confirmed to contain halos and or relics (Feretti et al. 2012), but the origin and evolution of this diffuse emission is still a matter of debate. Both types of diffuse emission are seen only in clusters undergoing mergers. A third class of diffuse radio emission, called mini-halos, is seen only in more relaxed, cool core clusters.

Radio halos are thought to be the result of either collisions between cosmic-ray protons and thermal protons (Dennison 1980) or particle acceleration through turbulence injected into the merging cluster system (see review by Petrosian & Bykov 2008).

Models for the formation of radio relics rely on the presence of a shock, driven by a cluster merger, within the X-ray gas. The two primary mechanisms for forming radio relics are (1) diffusive shock acceleration (DSA) through the Fermi-I mechanism and (2) adiabatic compression of fossil radio plasma by the merger shock. In the first scenario the relativistic electrons are the result of either acceleration of thermal electrons (Ensslin et al. 1998) or reacceleration of pre-existing cosmic ray particles (Kang & Ryu 2011) which have experienced multiple crossings of the shock front to gain energy. In the adiabatic compression scenario, the merger shock is thought to pass over and compress a cocoon of aged relativistic plasma where the high sound velocity inside the old radio plasma would inhibit the shock (Enßlin & Gopal-Krishna 2001). Compression of the cocoon would increase the magnetic field strength and energy density of the relativistic electrons within the cocoon. This would lead to a boost in the synchrotron luminosity of the emission during this "Flashing" phase of the model of Enßlin & Gopal-Krishna (2001). Such a re-ignited cocoon would thus become observable if it is sufficiently young that the cutoff frequency from losses remains above the observing frequency. Enßlin & Gopal-Krishna (2001) estimate that for re-ignition, the fossil plasma should not be older than 0.2 Gyr near the cluster center or up to 2.0 Gyr on the cluster outskirts prior to the shock passage.

The acceleration mechanism of relics may (in some cases) be differentiated by the radio spectrum. Shock accelerated or reaccelerated relics are expected to be fit to a power law spectrum while adiabatically compressed relics should have a strongly curved spectrum reflecting their pre-compression losses. Keshet (2010) has proposed a unified model for radio halo and relic formation based on a single secondary cosmic ray electron model, where the time evolution of both the magnetic fields and the cosmic ray distribution are taken into account to explain the origin of the diffuse emission.

We have recently detected an ultra steep spectrum (USS) diffuse radio source in A2443 (Cohen & Clarke 2011, hereafter CC11). In this paper we present results from a short *Chandra* observation of the system. This first pointed X-ray observation of this cluster reveals a disturbed ICM, with two X-ray surface brightness edges. One of the edges is consistent with a cold front, while the other edge is more suggestive of a shock edge. The spatial coincidence of the latter edge with the diffuse radio emission supports the interpretation of the diffuse radio emission as a shock-induced (compressed or reaccelerated) USS relic. We assume $H_o = 70$ km s$^{-1}$ Mpc$^{-1}$, $\Omega_M = 0.3$, and $\Omega_\Lambda = 0.7$ ($1'' = 1.95$ kpc at $z = 0.108$) throughout. Errors are given at the 68% confidence level unless otherwise stated.

## 2. THE GALAXY CLUSTER A2443

A2443, a rich cluster at an intermediate redshift of $z = 0.108$ (Struble & Rood 1999), and is dominated by two large galaxies near its center (Crawford et al. 1999). The cluster is also host to the powerful radio source 4C+17.89 which Crawford et al. associate with the fainter of the two central dominant galaxies.

Deep NRAO Very Large Array (VLA) radio observations of A2443 at 74, 325 and 1425 MHz reveal the presence of a diffuse USS radio source as well as three tailed galaxies (CC11). In Figure 1, we show the VLA 1425 MHz grayscale image of the cluster with source labels. Two of the tailed radio galaxies (A and B in Figure 1) are spectroscopically confirmed cluster members while the third source host (C in Figure 1) has a photometric redshift consistent with cluster membership and is identified by Crawford et al. (1999) as the brightest cluster galaxy (BCG). Source A displays classic narrow-angle-tail (NAT) morphology, source B may be a head-tail source or an NAT that was not resolved by CC11, while source C appears as a distinct core and small tail to the northeast. NAT sources are generally located in the outer regions of clusters which are dynamically complex (Bliton et al. 1998). The bending of the tails is a result of either ram pressure due to bulk motions from the merger event or the orbital velocity of the host galaxy. Given the very similar tail directions for sources A and B, it seems likely that the morphology is a result of ram pressure due to a merger with a northwest to southeast component.

Supporting evidence of a disturbed dynamical state in A2443 comes from the multi-color photometry of Wen et al. (2007) where 301 cluster member candidates (289 of them new candidates) are identified. Candidates within 2 Mpc of A2443 were found by Wen et al. (2007) to be distributed along a northwest to southeast axis, similar to the merger axis suggested by the radio tail orientation.

The USS source discovered in CC11 has a spectral index[7] between 74 MHz and 325 MHz of $\alpha_{74}^{325} = -1.7 \pm 0.1$ and a much steeper spectral index between 325 MHz and 1425 MHz of $\alpha_{325}^{1425} = -2.8 \pm 0.1$. The source has no clear optical counterpart and is extended over a linear extent of ~350 kpc if we assume it is at the redshift of the cluster. CC11 interpret the source as an USS radio relic. USS relics are found only in merging clusters and are thought to be connected to effects of merger shocks. Observations from the *ROSAT* All-Sky Survey (Truemper 1993) PSPC data revealed the presence of X-ray emission associated with the cluster, but had insufficient resolution to examine the cluster merger state (see Figure 10 of CC11).

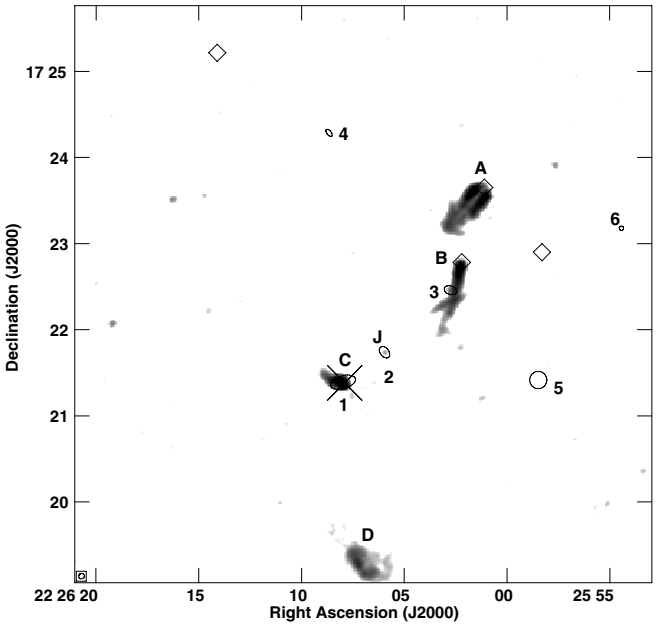


**Figure 1.** NRAO VLA 1425 MHz radio image in grayscale. The beam, with resolution of 4.00 × 3.75 arcsec, is shown in the lower left corner. Radio source labels follow the convention of CC11 and add new source J which is a faint radio source with an X-ray counterpart that is likely a background source. The six bright X-ray point sources discussed in Section 4.1 and Table 1 are indicated by the corresponding numbered black ellipses. The BCG from Crawford et al. (1999) associated with source C is indicated by a cross. The diamonds indicate the four spectroscopically confirmed cluster-member ellipticals that are within 1 mag in *I*-band of the BCG (Miller et al. 2002). Two of these cluster-member ellipticals are associated with the tailed radio galaxies A and B. The field of view is roughly 800 kpc on a side.

## 3. *CHANDRA* OBSERVATIONS

We observed A2443 with *Chandra* for 15.2 ks on 2010 August 20 (ObsID 12257). The cluster core was placed on the back-side-illuminated ACIS-S3 CCD and the data were taken in VFAINT mode. All data were reprocessed from the level 1 event files using the latest calibration files (as of CIAO 4.3). CTI and time-dependent gain corrections were applied. LC_CLEAN was used to remove background flares.[8] The energy range for the flare cleaning was 2.5–7 keV as recommended in the COOKBOOK[9] and the filtering was done on the ACIS-S1 and ACIS-S3 CCDs with the cluster contribution on the S3 CCD masked. The mean event rate was calculated from a source free region using time bins within $3\sigma$ of the overall mean, and bins outside a factor of 1.2 of this mean were discarded. There were no periods of strong background flares. The resulting cleaned exposure time was 14.5 ks.

[7] Spectral index ($\alpha$) is defined such that $S_\nu \propto \nu^\alpha$ for a source with measured flux $S$ at frequency $\nu$.

[8] http://asc.harvard.edu/contrib/maxim/acisbg/

[9] http://asc.harvard.edu/contrib/maxim/acisbg/COOKBOOK

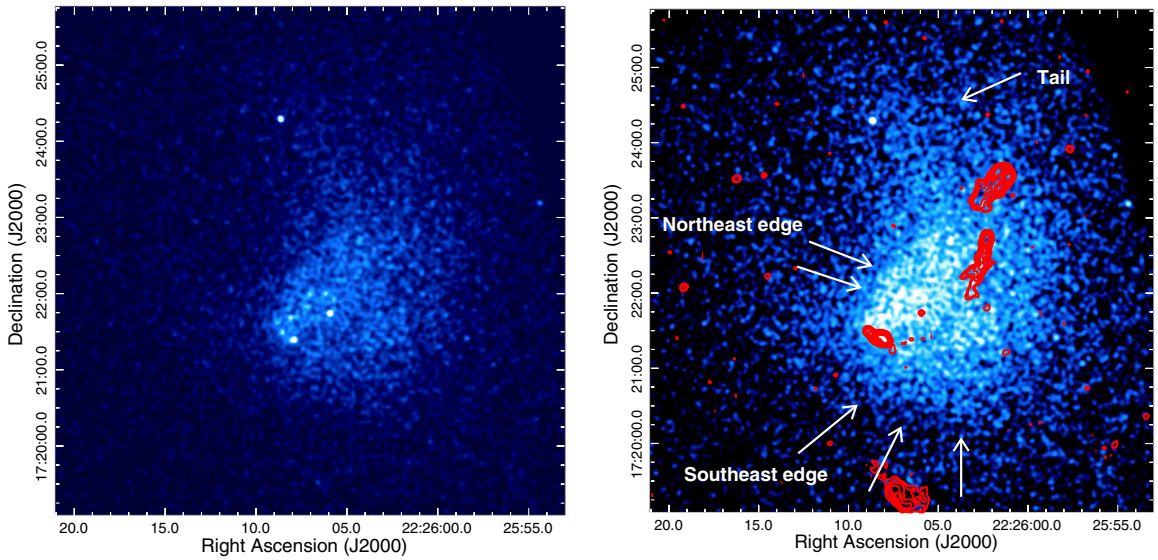


**Figure 2.** Background corrected 0.3–7.0 keV *Chandra* ACIS-S images of A2443 smoothed with a Gaussian of 1.″5. Left: the bright central ICM appears disturbed with an elongation along a southeast to northwest direction. Also visible are several compact X-ray sources including two near the center of the ICM. Right: same as the left panel but with a logarithmic stretch to highlight the features of the diffuse emission. The northern tail as well as the northeast and southeast edges (all marked by arrows) are clearly visible. Overlaid are the 1425 MHz contours corresponding to the emission seen in Figure 1. Both images show a region of 800 kpc on a side.

(A color version of this figure is available in the online journal.)

Diffuse emission from A2443 fills almost the entire S3 field of view. We therefore used the CALDB[10] blank sky background files appropriate for the observation, normalized such that the count rate in the 10–12 keV band matched the observed rate. Normalizations were computed using data from the S3 and S1 chips with point sources and regions of bright, diffuse cluster emission excluded. Since bright emission from A2443 fills most of the S3 chip, the normalization was largely determined by data from the S1 chip. To generate exposure maps, we assumed a MEKAL model with $kT = 5.0$ keV, Galactic absorption of $N_{\rm H} = 5.21 \times 10^{20}$ cm$^{-2}$ (Dickey & Lockman 1990), and an abundance of 30% solar at a redshift $z = 0.108$, which is consistent with typical results for the extended emission from detailed spectral fits (see Section 5).

## 4. X-RAY IMAGING ANALYSIS

The background corrected 0.3–7.0 keV smoothed ACIS-S *Chandra* image of the central 800 kpc of A2443 is shown in Figure 2. The cluster is dominated by a large region of diffuse emission with no obvious compact core. The main characteristics seen for the diffuse emission are the edges to the northeast and southeast of the core as well as a faint diffuse tail extending to the north. Figure 2 contains two panels with different intensity scales to bring out the brighter emission in the cluster core on a linear scale (left panel) and the fainter extended emission using a logarithmic scale (right panel). The left panel clearly shows the compact sources and central cluster emission including an inner edge to the northeast while the right panel reveals the details of the northern tail and the outer southeast surface brightness edge. We label the main diffuse ICM features discussed in this paper within the right panel of Figure 2 and also overlay the VLA 1425 MHz radio contours on this panel. In Figure 3 we show an overlay of the smoothed X-ray contours on the SDSS *r*-band image of A2443. We also include labels from Figure 1 for reference.

[10] http://cxc.harvard.edu/caldb/

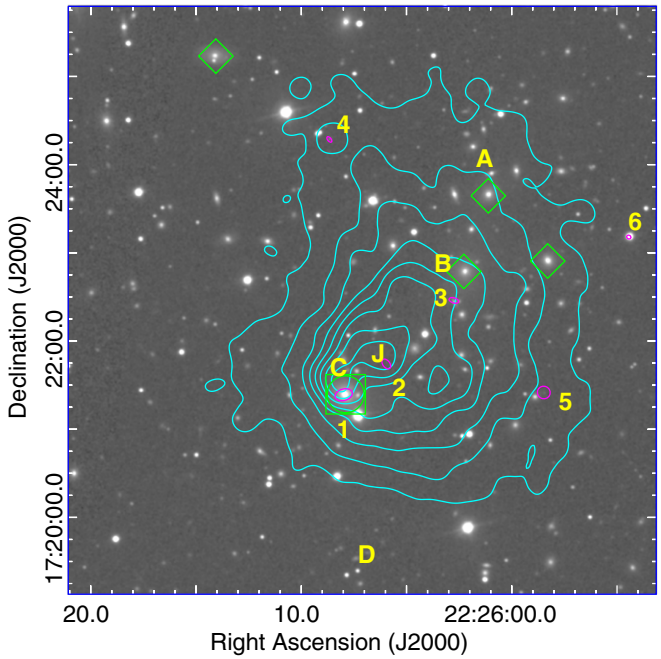


**Figure 3.** Sloan Digital Sky Survey (SDSS) *r*-band image of A2443 with smoothed *Chandra* 0.3–7.0 keV X-ray contours overlaid in cyan. Labels are as in Figure 1 except we have changed the BCG cross to a circle-box to avoid covering the optical emission.

(A color version of this figure is available in the online journal.)

### 4.1. Compact Sources

We searched for point sources on the ACIS-S3 chip using the wavelet decomposition program WAVDETECT (Freeman et al. 2002). We used a range of spatial scales covering 1, 2, 4, 8, and 16 pixels where the images were binned by a factor of two such that 1 pixel is roughly 1″. Sources were visually confirmed in the X-ray images. We found a total of 6 sources (labeled in Figures 1 and 3) and list details of these sources in Table 1.

**Table 1**
*Chandra* Compact X-Ray Sources

| Source | R.A. (J2000) | Decl. (J2000) | Redshift | Optical ID | Radio ID | XAssist Flux (erg s$^{-1}$ cm$^{-2}$) |
|---|---|---|---|---|---|---|
| 1 | 22 26 07.98 | +17 21 23.47 | 0.107 | BCG | C | $2.20 \times 10^{-14}$ |
| 2 | 22 26 05.96 | +17 21 44.67 | 0.227 | T96 | J | $1.75 \times 10^{-14}$ |
| 3[a] | 22 26 02.75 | +17 22 27.36 | 0.115 | T06 | B tail | ... |
| 4 | 22 26 08.66 | +17 24 17.15 | 0.115 | ... | ... | $2.22 \times 10^{-14}$ |
| 5 | 22 25 58.48 | +17 21 25.00 | ... | Star | ... | ... |
| 6 | 22 25 54.43 | +17 23 10.72 | ... | A-star | ... | $7.62 \times 10^{-15}$ |

**Notes.** Column 1 lists the source ID number, Columns 2 and 3 are the right ascension and declination in J2000 measured from *Chandra*, Column 4 is the source photometric redshift (if known), Column 5 is the optical ID where BCG indicates the brightest cluster galaxy as indicated by Crawford et al. (1999) and TNN refers to galaxy number NN in the catalog of Trujillo et al. (2001), Column 6 is the associated radio source ID from Cohen & Clarke (2011) or this paper, and Column 7 is the XAssist flux in the 0.3–8.0 keV band (Ptak & Griffiths 2003).
[a] Source 3 is the lowest significance source (2.96) from WAVDETECT.

Three of the brightest sources are easily visible in Figure 2. Two bright compact X-ray sources are near the cluster center and the third is visible near the tail to the north. The eastern central point source is co-incident with the cD galaxy PCG 068859 at a photometric redshift of $z = 0.107$ (Slee et al. 1994). This galaxy (identified as the BCG by Crawford et al. 1999) is host to the head-tail radio source C identified by CC11 (see Figure 3). The western bright central X-ray point source is co-incident with a faint compact 1425 MHz radio source labeled source J in Figure 1 as well as a faint optical galaxy seen in Trujillo et al. (2001). Based on the faint absolute magnitude ($I$-band magnitude of $-16.99$) it is unlikely that this galaxy is an elliptical cluster member and thus it is most likely an unrelated faint background object detected at all three wavelengths. The SDSS photometric redshift of $z_{\rm phot} = 0.227 \pm 0.091$ further supports the background source identification. The bright northern X-ray source has no associated radio counterpart but the optical counterpart has a photometric redshift of $z_{\rm phot} = 0.115 \pm 0.027$ from the SDSS DR8, indicating that it is likely a cluster member. Of the remaining three fainter X-ray sources, one is co-incident with the tail of galaxy B in the notation of CC11. This source is also co-incident with object 6 of Trujillo et al. (2001) and is likely an elliptical cluster member based on the measured magnitude, although we note that there are two optical IDs in the SDSS within the X-ray source region and this is the lowest significance WAVDETECT source. The X-ray source to the west of the cluster core has no radio counterpart and is identified in the SDSS DR8 as a star. The final X-ray source to the NW of the cluster is coincident, although slightly off-center, to a source in the USNO UCAC3 catalog (Zacharias et al. 2010). The magnitudes listed in the catalog show that the source is too bright optically to be a cluster member and the colors are more consistent with an A-type star.

### 4.2. Extended Emission

In Figure 4 we show details of the diffuse ICM with the 74 MHz radio contours from CC11 overlaid. The X-ray image was made by adaptively binning using the Voronoi tessellation technique of Diehl & Statler (2006) with a signal-to-noise ratio (S/N) of 5. The compact X-ray sources have been masked in the process. The main X-ray features visible are the tear-drop shaped region of diffuse X-ray emission with sharp edges to the northeast and southeast of the core, and more gradual surface brightness decrease to the west. The overall complex shape of the ICM emission and the lack of a compact core are both consistent

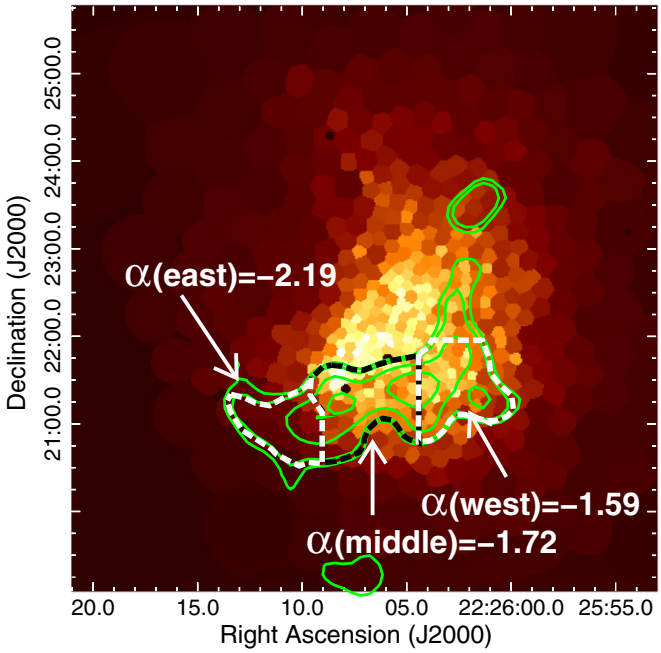


**Figure 4.** *Chandra* 0.3–7.0 keV image of the central region of A2443 adaptively binned using Voronoi tessellation with a S/N = 5 to highlight the diffuse emission. Overlaid are VLA 74 MHz contours in green. The three contiguous dashed areas show the regions where the spectral index values discussed in Section 6 were calculated. The middle region (indicated in black) contains the compact source C. The spectral index between 330 MHz and 74 MHz for each region is indicated.

(A color version of this figure is available in the online journal.)

with a cluster undergoing a merger. The diffuse intracluster X-ray emission extends over a region of roughly 600 kpc × 550 kpc and is elongated in the north–south direction on large scales and in the northwest to southeast direction within the central 150 kpc.

The sharp inner northeast edge has no associated radio emission while the southeast edge is coincident with the location of the USS radio emission discovered by CC11. The connection between the USS radio emission and southeast edge suggests that this may be a shock front which has compressed fossil radio plasma or reaccelerated relativistic particles in this region. The northern portion of the cluster is dominated by an X-ray tail that arcs toward the northeast and may represent ram-pressure stripped material from a merger, or the tail may be the outer

portion of the spiral excess from a sloshing core. We discuss these possibilities further in Section 7.

## 5. X-RAY SPECTRAL ANALYSIS

### 5.1. Average Cluster Spectrum

The ICM in A2443 shows evidence of an extended, disturbed morphology, consistent with a dynamically complex merging system. In order to look at the global cluster properties we have fit the total intracluster emission (which covers the majority of the ACIS-S3 CCD) using a circular region of radius 330 kpc centered on the bright central emission. For all model fitting we have fixed the absorption at the Galactic value. Using a single temperature absorbed APEC model, we find a best fit temperature of $kT = 7.12^{+0.38}_{-0.33}$ keV and abundance[11] of $Z = 0.37^{+0.09}_{-0.09}\ Z_{\odot}$, with a reduced $\chi^2$ of $\chi^2_{\nu} = 227.9/201$. Allowing for non-solar abundances in the VAPEC model results in a reduced $\chi^2$ of $\chi^2_{\nu} = 223.8/200$ which is a marginally significant improvement according to the $F$-test. The best-fit VAPEC model gives $kT = 7.00^{+0.38}_{-0.29}$ keV, and abundances of Si $= 1.35^{+0.50}_{-0.49}$ and Fe $= 0.36^{+0.09}_{-0.09}$ with all other elements constrained and fixed at 0.4. Deeper X-ray observations are required to confirm and/or improve fits to non-Solar abundances.

### 5.2. Temperature Map

We have constructed a temperature map of A2443 using the method employed by Randall et al. (2008). For each temperature map pixel, we extracted a spectrum from a circular region containing roughly 1000 net counts after background subtraction. The extraction regions ranged in radius from about 55″ (∼107 kpc) in the bright central regions to 238″ (∼464 kpc) in the faint outer regions to the east. This mapping process results in extraction regions that are significantly larger than the pixels shown in the resulting temperature map, therefore the map pixels are not independent, and the maps are effectively smoothed. For each temperature map pixel, the resulting spectrum was fitted in the 0.6–8.0 keV range with an absorbed APEC model using XSPEC, with the abundance allowed to vary.

The temperature map and associated $1\sigma$ upper and lower limits are shown in Figure 5. The main purpose of the temperature map is to identify interesting features for further study. Once features are identified, we fit extracted spectra of the regions to determine the temperatures and assess the statistical significance of the features.

The temperature map shows two distinct temperature peaks, one 67″ (∼130 kpc) southwest of the core, the other 82″ (∼160 kpc) east of the core. We extracted spectra from a 30 arcsec (58.5 kpc) radius region centered on the southwestern temperature peak and from an identical, non-overlapping region just northwest of the peak in a region of comparable surface brightness. We fitted each spectrum with an absorbed APEC model, with the abundance fixed at 30% solar. We find temperatures of $kT_{\rm sw-peak} = 18.1^{+8.4}_{-5.1}$ keV for the temperature peak and $kT_{\rm sw-offset} = 6.8^{+1.2}_{-0.9}$ keV for the adjacent region. The background makes up <6% of the total emission in this region, so that the systematic uncertainties associated with the background do not significantly affect the error budget. Thus, the temperature enhancement at the southwestern peak is significant at $\sim 2.2\sigma$. The temperature peak is equally well-described by an absorbed power-law model, with a photon index of $\Gamma = 1.40^{+0.06}_{-0.06}$. Due to the low number of counts and the implied high temperature of the thermal plasma, we were unable to distinguish between these two models.

Performing a similar test for the eastern temperature peak by extracting spectra from a 54 arcsec (∼105 kpc) radius region centered on the peak and from an identical, non-overlapping region just south-southwest of the peak, we find temperatures of $kT_{\rm e\text{-}peak} = 20.9^{+29.4}_{-9.0}$ keV and $kT_{\rm e\text{-}offset} = 5.5^{+2.3}_{-1.4}$ keV. This implies that the temperature enhancement at the eastern peak is significant at $\sim 1.7\sigma$. However, the background makes up ∼30% of the total emission in these lower surface brightness regions, so that systematic uncertainties in the background contribute significantly to the total error budget. Including a 5% systematic uncertainty in the background normalization, we find that $kT_{\rm e\text{-}peak} = 20.9^{+36.0}_{-10.0}$ keV and $kT_{\rm e\text{-}offset} = 5.5^{+3.2}_{-1.6}$ keV. Thus, including the systematic uncertainty in the background, the eastern temperature peak is significant at $\sim 1.5\sigma$. As with the southwestern temperature peak, the spectrum is equally well-modeled with an absorbed power-law model, with $\Gamma = 1.34^{+0.08}_{-0.08}$ (including the systematic background uncertainty).

Since we cannot distinguish between thermal emission and non-thermal power law emission in the regions of the high temperature peaks, a concern is that unresolved sources are driving the hard spectra (and thus, high temperatures) in these regions. This is especially a concern for the eastern temperature peak, where the X-ray surface brightness is relatively low. We therefore considered how many unresolved sources would be required to drive the cooler temperature measured adjacent to the eastern temperature peak ($kT_{\rm e\text{-}offset} \approx 5.5$ keV) up to be consistent with the high peak temperature ($kT_{\rm e\text{-}peak} \approx 20.9$ keV) at $1\sigma$ when fitting a single temperature model by performing XSPEC simulations. We assume background sources that are just below the $5\sigma$ detection limit, with a flat spectral index of $\Gamma = 0.3$, roughly the lower limit of spectral indices observed in individual sources in deep blank sky observations with *Chandra* (e.g., Brandt et al. 2001). These are conservative assumptions, since the higher detection limit allows for brighter unresolved sources, which will affect the blended spectra more significantly, and flatter spectral indices contribute relatively more photons at higher energies, also more significantly affecting the blended spectrum. We find that three such sources are required within the 54 arcsec radius extraction region for the eastern temperature peak to bring the temperature fitted for the blended spectrum into agreement with the observed value, whereas the relationship between the number of background sources $N$ above a given flux $S$ measured from *Chandra* Deep Field observations (Brandt et al. 2001) predicts ∼0.3 sources in the region of the eastern temperature peak. Thus, while we cannot rule out the possibility of contamination from unresolved point sources giving rise to the observed temperature peaks, we conclude that this is unlikely. We discuss a possible scenario for the hotspots in Section 7.

The temperature map also shows a cool plume of gas extending to the north (Figure 5), in the region of the bright tail seen in the X-ray image (Figure 2). This feature is heavily smoothed in the temperature map, owing to the low number of total net counts in this region. To test the significant of this feature, we extracted spectra from a 75 arcsec by 47 arcsec (∼146 × 92 kpc) elliptical region covering the bright tail and from an identical region in the fainter area northeast of the bright cluster core (just north of the eastern temperature peak). For the tail, we find $kT_{\rm tail} = 4.8^{+0.5}_{-0.5}$ keV and an abundance of $Z_{\rm tail} = 0.3^{+0.2}_{-0.2}\ Z_{\odot}$. For the region east of the tail, we find

[11] We report abundances relative to solar abundances assuming the Anders & Grevesse (1989) abundance measurements.

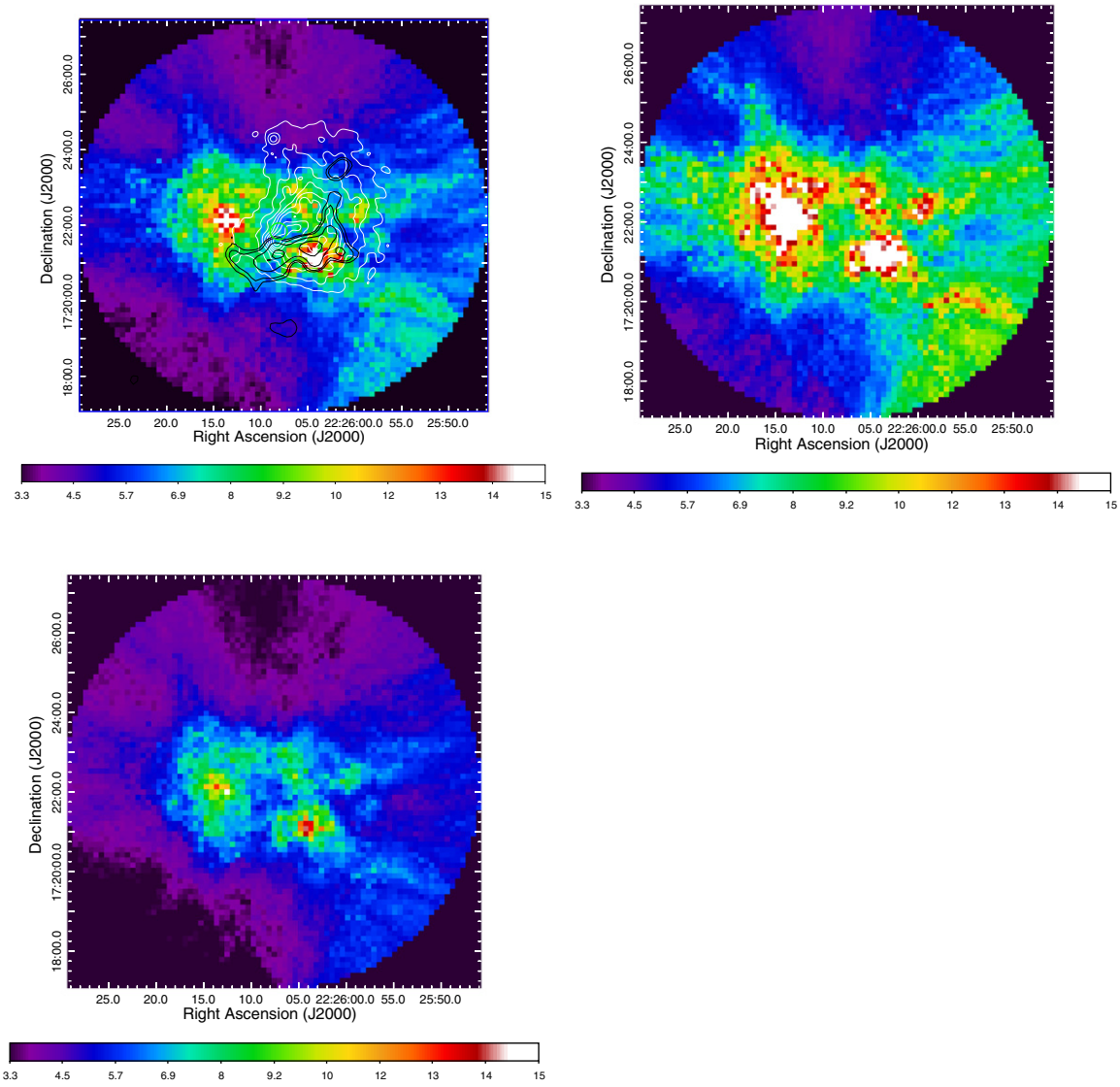


**Figure 5.** Top left: *Chandra* temperature map of A2443 showing two hot regions straddling a cooler region near the cluster center. The temperature at each pixel is determined from a spectral extraction region containing at least 1000 background subtracted counts. Colorbars for all plots show the temperature range in keV. VLA 74 MHz contours from Cohen & Clarke (2011) are shown in black and the smoothed *Chandra* 0.3–7.0 keV contours are shown in white. Top right: temperature error map ($1\sigma$) for the upper limits to the temperature fits. Bottom left: temperature error map ($1\sigma$) for the lower limits to the temperature fits.

(A color version of this figure is available in the online journal.)

$kT_{\text{tail-offset}} = 8.4^{+4.8}_{-2.2}$ keV ($kT_{\text{tail-offset}} = 8.4^{+6.9}_{-2.7}$ keV including a 5% systematic uncertainty in the background, as above). The abundance could not be constrained in this off-tail region, and was fixed at 30% solar. Thus, the cooler temperature in the region of the tail is marginally significant, at $1.3\sigma$.

We show in Figure 6 the pseudo-entropy and pseudo-pressure maps for A2443. The pseudo-pressure map shows evidence of a jump near the location of the radio relic which would be expected if this emission is associated with an X-ray shock. The main features of the pseudo-entropy map are the low entropy gas associated with the cooler cluster-center gas as well as a tail of low entropy gas to the north that traces the northern X-ray tail seen in Figure 2. The lack of a clear jump at the relic location in the pseudo-entropy map is not surprising since the entropy jump for a low to moderate Mach number shock is much less than the associated pressure jump. Given the large extraction regions in the temperature map, the entropy jump may be further masked by the blending of the central cool gas into the shock region.

### 5.3. Edge Analysis

Analysis of Figure 2 reveals two possible X-ray edges, one to the northeast and one to the southeast of the bright central region. To characterize the apparent X-ray edges we have set two large partial annuli (shown as dashed green regions in Figure 7) on either side of the edges and fit the temperature using an APEC model. Results from this analysis suggest that the southeast edge may be a shock with inner hot shock-heated gas temperature of $kT_{\text{in}} = 10.9^{+4.2}_{-2.3}$ and outer undisturbed gas temperature of $kT_{\text{out}} = 3.3^{+1.0}_{-0.6}$ keV. The northeast edge on the other hand has a cool inner temperatures of $kT_{\text{in}} = 6.5^{+0.9}_{-0.7}$ and hotter gas outside with $kT_{\text{out}} = 9.3^{+2.7}_{-1.6}$ keV. The presence of cool gas inside and hotter gas outside suggests that this may be a "cold front" edge rather than a shock. Cold front edges are contact discontinuities which are observed in both relaxed and merging clusters (see review by Markevitch & Vikhlinin 2007). We discuss the potential cold front further in Section 7.2 in connection with the northern X-ray tail.

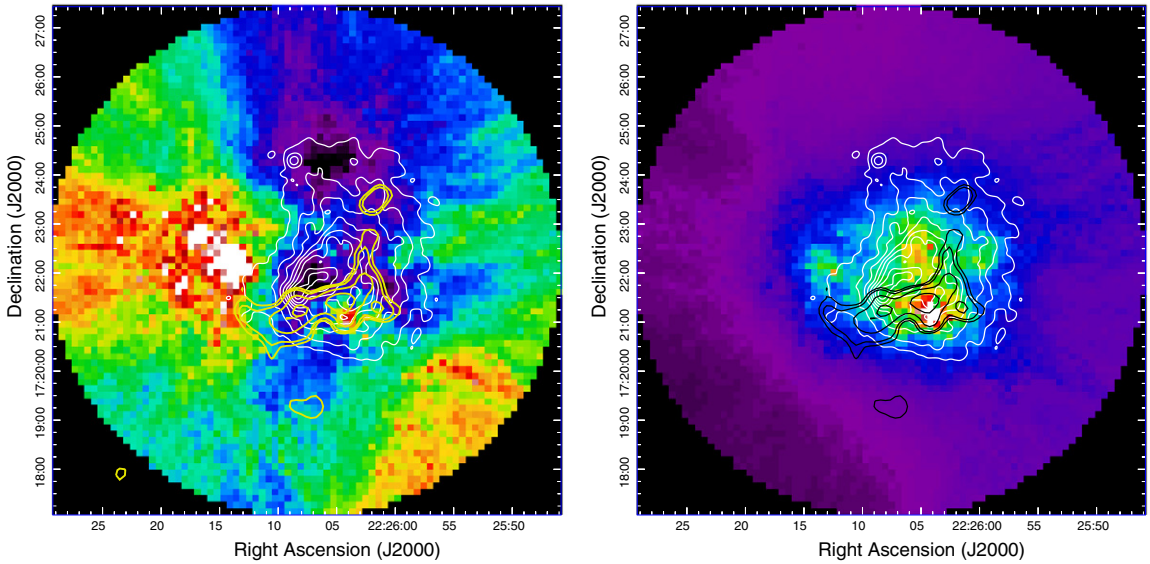


**Figure 6.** The pseudo entropy (left) and pressure (right) maps, in arbitrary units (white/red regions are high and purple/black regions are low). The entropy map was calculated as $kTA^{-1/3}$ and the pseudo pressure map as $kTA^{1/2}$, where $A$ is the APEC normalization scaled by the area of the extraction region and $kT$ is the best fit temperature. Note that the radial extensions are due to smoothing artifacts in the maps that result from the fact that the extraction radii generally grow with distance from the bright central region. The entropy map shows low entropy gas associated with the cluster core and northern tail. The pseudo-pressure map shows a high pressure region near the relic which may indicate the presence of a shock. White contours show the smoothed *Chandra* 0.3–7.0 keV emission and the VLA 74 MHz contours from Cohen & Clarke (2011) are shown in yellow on the left panel and black on the right panel.

(A color version of this figure is available in the online journal.)

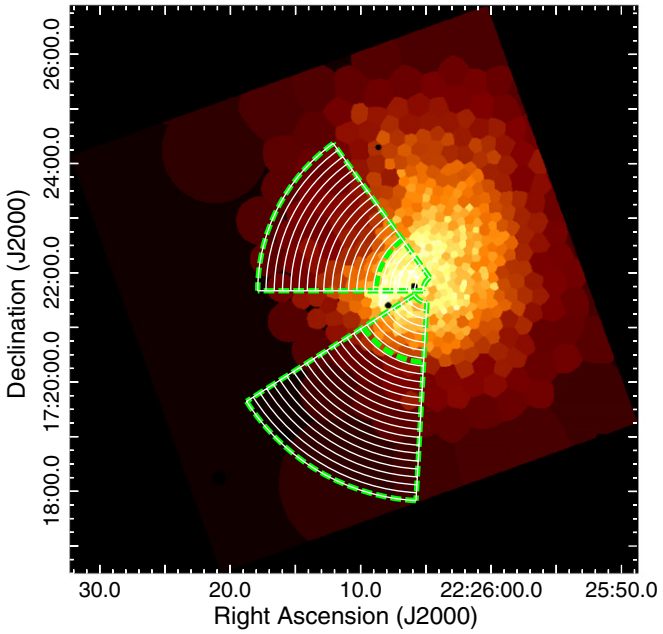


**Figure 7.** Voronoi tessellation image of the full ACIS-S3 CCD with the two surface brightness sectors overlaid in white. The inner and outer temperature wedges on either side of the two edges (discussed in Section 5.3) are overlaid as dashed green regions.

(A color version of this figure is available in the online journal.)

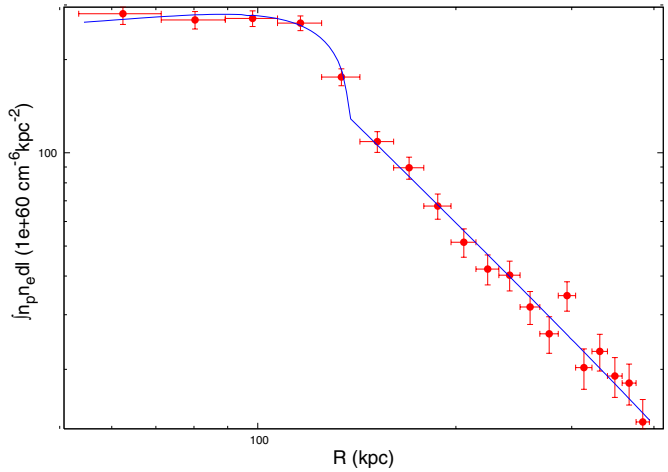


**Figure 8.** Edge fit to the X-ray surface brightness (data points) across the northeast "cold front" edge. The best-fit discontinuous power-law density model is shown as the curve.

(A color version of this figure is available in the online journal.)

We have extracted surface brightness profiles across both edges using the two pie-shaped sectors shown in Figure 7. The sectors are defined to be centered on the center of curvature of the X-ray edges rather than the ICM center or the BCG. The resulting profiles are shown as the data points in Figures 8 and 9 for the northeast and southeast edges respectively. The surface brightness profiles toward each edge were fitted by projecting a three-dimensional density model consisting of two power-laws separated by a discontinuous jump as described in Randall et al. (2009). Due to the short exposure, there were insufficient counts to fit the temperature or abundance profiles across the edges. Each surface brightness profile was fit assuming $kT = 7$ keV and an abundance of $Z = 0.5\ Z_{\odot}$ that reflects an intermediate value between the core and total abundance values. We note that using the pre- and post-edge temperatures do not significantly change the calculated density jumps.

The northeast "cold front" edge is consistent with a density jump of 1.5–1.8 and the best-fit model is shown as the solid line in Figure 8. We note however that this model fit has a non-physical positive density slope inside the edge which is likely the result of applying a spherically symmetric model to this complex system. The breakdown of the spherical symmetry assumption

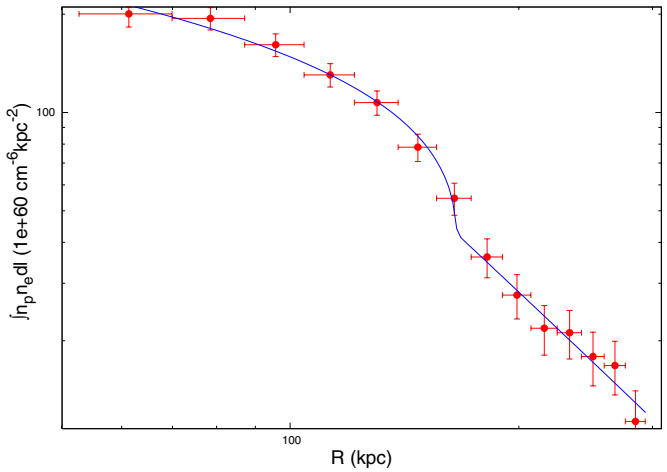


**Figure 9.** Edge fit to the X-ray surface brightness (data points) across the southeast "shock" edge. The best-fit discontinuous power-law density model is shown.

(A color version of this figure is available in the online journal.)

may impact our fitting results but we note that the detection of the edge is not impacted by this assumption. Deeper X-ray data are needed to extract the profile in smaller bins near the edge to minimize the effect of the spherical symmetry assumption.

The southeast "shock" edge model fit is shown in Figure 9 and the associated best-fit density jump is in the range of 1.2–1.8. The best-fit density discontinuity of 1.6 would be consistent with a Mach number of $\mathcal{M} \approx 1.4$ shock. The apparent temperature jump we measure above is a factor of 3.3 which would imply a stronger shock ($\mathcal{M} \approx 2.8$) than measured by the density jump. Ideally we would like to measure the temperature jump using small bins on either side of the edges in order to clearly distinguish the jumps due to the edges from the underlying large-scale trend with radius. Unfortunately we are only able to measure the temperature jump in very large pie bins and thus there may be large systematic errors in the measurements. Other effects such as projection and non-equipartition could also reduce the observed temperature jump. Given the large uncertainties in these measurements due to the short exposure and low counts outside the bright core, the Mach number is still very uncertain. Despite the uncertainty, both the density and temperature measurements suggest the presence of a shock near the outer edge of the USS radio source. A detailed analysis of the edges to better constrain the parameters will require much deeper *Chandra* observations.

## 6. RADIO SPECTRAL ANALYSIS

The A2443 radio relic emission is very steep spectrum and shows spectral curvature in the integrated spectrum (CC11). These spectral characteristics suggest that this source is most likely the result of compression of fossil radio plasma by a merger shock. The steep, curved spectral index is characteristic of a plasma which is heavily affected by synchrotron and inverse Compton losses (Enßlin & Gopal-Krishna 2001). Shock reacceleration can produce steep spectrum emission but the spectrum is well-fit by a power-law that connects the observed injection spectral index to the shock Mach number (Pinzke et al. 2013). We therefore suggest that the A2443 emission can be classified as an adiabatically compressed radio phoenix. Other examples of sources which fall within this class are the four USS sources studied by Slee et al. (2001), as well as the more recent sources presented by van Weeren et al. (2009a, 2009b, 2011), Ogrean et al. (2011), and Kale & Dwarakanath (2012). The spatial co-incidence of the USS radio source with the possible X-ray shock in A2443 provides further support for the relic interpretation.

If the radio emission results from adiabatic compression of fossil radio plasma, then the fossil plasma should not be older than 0.2–2.0 Gyr prior to the shock passage, depending on the external pressure (Enßlin & Gopal-Krishna 2001). Typical relics generated through adiabatic compression are generally limited to scales of order 100 kpc or less due to radiative energy losses sustained by the relic over the timescale needed to compress a large system. Most relics are observed at GHz frequencies where we would expect radiative losses to remove the electrons responsible for the emission on time scales of a few tens of Myr after shock passage for typical relic magnetic field strengths. Observations at lower frequencies, such as presented here for A2443, are able to trace the relic emission from older regions of compression. We might therefore expect to see both larger adiabatically compressed relics as well as a spectral gradient across the relic due to aging behind the region of current compression.

It is possible that the A2443 relic is the result of a more complex scenario such as a mix of compression and simultaneous reacceleration of pre-existing relativistic particles. In order to better characterize the relic we use the radio data of CC11 to investigate the spatial distribution of the spectral index along the ∼350 kpc length the relic. We note that we do not currently have sufficient spatial resolution across the ∼100 kpc width of the relic at multiple frequencies to look for the spectral gradient along that direction.

We have divided the steep spectrum emission identified by CC11 as the relic region into three contiguous, roughly equal area regions across the east–west axis of the emission. We show these regions overlaid on the 74 MHz contours in Figure 4. We have clipped the 74 MHz A configuration image and matched-resolution 330 MHz B configuration image of CC11 at the $5\sigma$ level for the respective data sets. Both data sets have been convolved to an identical circular beam size of $23\farcs4$. The middle of the three regions contains emission from the compact source C while the other two regions (east and west) are free of contamination from discrete sources. We have measured the total flux within each of the three regions at 74 and 330 MHz and corrected the flux measured in the middle region for the excess emission from source C. Errors on the flux measurements for each region include contributions from the rms noise as well as the addition of a flux scale uncertainty of 3% at 330 MHz and 6% at 74 MHz. These flux measurements and uncertainties result in spectral index measurements between 74 and 330 MHz of $\alpha_{\rm east} = -2.19 \pm 0.07$, $\alpha_{\rm middle} = -1.72 \pm 0.07$, and $\alpha_{\rm west} = -1.59 \pm 0.05$. These values are consistent with a spectral steepening from west to east that is significant at roughly the $7\sigma$ level.

This spectral steepening eastward across the relic may be a reflection of the original uncompressed spectrum that was more aged (steeper) on the eastern edge compared to the western edge. Such a steepening could be consistent, for example, with what would be expected for spectral aging of plasma in the tail of source B where the plasma ages eastward, away from the head. Additional spectral steepening would be expected if the shock moved across the length of the relic from the east toward the west. Alternatively, the spectral variation along the length of the relic may be due to shock acceleration with a variation of

the Mach number along the relic, or due to a spectral gradient of a pre-existing population of relativistic electrons that was reaccelerated by the shock passage.

A detailed study of the spatial distribution of the spectrum and spectral curvature will be presented in an upcoming paper that incorporates additional new high-resolution, multi-frequency radio observations from the Giant Metrewave Radio Telescope and the VLA.

## 7. DISCUSSION

We present an analysis of the first pointed X-ray observation of the cluster A2443 that is host to an USS radio source. Our new *Chandra* observation reveals that the ICM is elongated along a NW to SE axis in the inner regions, and has an apparent X-ray tail to the north in the outer regions. In addition, the X-ray surface brightness shows two clear edges in the central region with an inner edge to the NE and outer edge to the SE. In this section, we discuss the implications of our analysis in more detail.

### *7.1. A2443 Environment*

The inner ICM elongation from NW to SE is similar to the optical galaxy distribution of photometrically determined cluster member galaxies in a 2 Mpc region surrounding A2443 (Wen et al. 2007). We also note that there is a second galaxy cluster, ZwCl 2224.2+1651, with associated X-ray emission from *ROSAT*, that is located roughly 2.7 Mpc SE of A2443. Although this system has no spectroscopic redshift measurements, there are numerous photometric redshifts of galaxies within the region of this system that are consistent with the redshift of A2443 (Wen et al. 2007). In addition, there appears to be a relatively higher fraction of blue galaxies within the SE cluster which Wen et al. (2007) interpret as possibly resulting from recent star formation triggered by the on-going interaction with A2443. If the systems are undergoing a merger it is not clear from the current data what stage the merger is in. Based on the fact that there is a concentration of galaxies associated with the X-ray emission for the southern cluster, it may be in the early stages of infall (possibly along a filament) since we would expect ram pressure stripping of the X-ray emission from the southern system for any late stage encounter with A2443.

In order to further investigate the merger state of A2443, we have searched for redshift measurements of the galaxies in the vicinity of the cluster. We find that there are four spectroscopically confirmed cluster-member ellipticals that are within one magnitude in the *I*-band of the BCG identified by Crawford et al. (1999). These systems (identified in Figure 1) are located in a clump of three sources to the NW of the BCG and a fourth elliptical to the NE of the BCG.

### *7.2. Northern X-Ray Tail*

The outer X-ray tail seen to the north in A2443 arcs toward the NE of the cluster and is reminiscent of the tails seen for example in the infall of M86 into the Virgo Cluster (Randall et al. 2008), the early stage cluster merger in A115 (Gutierrez & Krawczynski 2005) and the intermediate stage cluster merger in A1201 (Ma et al. 2012). These tails have been interpreted as ram pressure stripped subhalos that consist of material stripped from the host systems as it passes through a diffuse external ICM.

We consider two possible ram pressure stripping scenarios for the northern tail of A2443. The first scenario we consider is the case where the tail may be stripped material from the cluster as it falls into the ICM of another system. We have searched the *ROSAT* All-Sky images in the region near the cluster to try to identify a potential stripping medium. The only nearby cluster is ZwCl 2224.2+1651, discussed above, which is likely associated with the *ROSAT* Bright Source Catalog source 1RXSJ 222715.9+17035 (Voges et al. 1999). At the projected distance of 2.7 Mpc, it seems unlikely that the tail in A2443 could be stripped material from the interaction with the distant system. If ZwCl 2224.2+1651 was responsible for stripping A2443, then the virial radius would need to be nearly 3 Mpc, as would be expected only for very massive clusters. Based on the X-ray emission, if the SE cluster is at the same redshift as A2443 then it must be significantly less massive than A2443 and thus could not be responsible for ram-pressure stripping the A2443 ICM.

The second ram pressure stripping scenario we consider for the tail is that A2443 is a binary merger system that is currently in an intermediate merger stage. If we consider two merging systems that have roughly equal masses, then the northern tail may be at least partially composed of stripped material from one or both of the merging subhalos. An additional component of the tail could come from merger-induced sloshing which is discussed below. Simulations of equal-mass mergers shown in Poole et al. (2006) reveal evidence of stripped X-ray tails with morphology very similar to A2443. The lack of two distinct X-ray cores in the cluster, together with the X-ray core elongation suggest that the merger is most likely in an intermediate stage, after both cores have disrupted, but before they merge and relax. The presence of multiple bright elliptical galaxies associated with A2443 supports the intermediate stage binary merger scenario.

An alternative scenario for the northern tail of A2443 is that it is an extended sloshing spiral resulting from the off-axis passage of a perturbing subcluster. Hydrodynamic simulations show that interactions with a passing subcluster can displace the cold central gas from the minimum of the cluster potential. The cold gas will overshoot the dark matter core as it falls back in, leading to the sloshing effect (Ascasibar & Markevitch 2006). Observationally, the X-ray signature of a sloshing core is a large spiral-shaped plume of cool, high metallicity gas running outward from the cluster core. Such sloshing spirals are seen in numerous cool core systems (e.g., A2029, Clarke et al. 2004; A2052, Blanton et al. 2011; Laganá et al. 2010).

The majority of cool-core clusters with deep X-ray data show the presence of "cold fronts," generated by sloshing, which trace the edges of the sloshing spiral (Markevitch & Vikhlinin 2007). We show that the northern tail of A2443 seen in Figure 5 is associated with a cool plume of gas although we caution that spectral fitting of the tail and an off-tail region (discussed in Section 5.2) indicate that the cooler temperature in the tail region is only significant at the $1.3\sigma$ level. Nevertheless, if the outer edge of the tail in A2443 is the signature of a sloshing spiral, then the sloshing spiral extent would be roughly 400 kpc. In this scenario, the inner edge we detect to the NE of the core would simply be a cold front that traces a portion of the inner region of the sloshing spiral near the core. This interpretation of the edge is consistent with our temperature estimates discussed in Section 5.3.

Numerous clusters show evidence of multiple cold fronts or sloshing features that extend from a few 10's of kpc out to 200–300 kpc with recent evidence in Perseus of an extent up to a Mpc (Simionescu et al. 2012). Although our current X-ray data are not sensitive enough to trace the full sloshing spiral

(if it exists) we note that the sloshing extent is similar to recent results from deep *Chandra* observations of A2029 which show a 400 kpc spiral, the largest *continuous* sloshing spiral known to date (Paterno-Mahler et al. 2013). In the case of A2443, we may be viewing the spiral at some angle to the line of sight (rather than face on) and thus would expect a more complex X-ray signature than expected for face on, as shown in the simulations of ZuHone et al. (2013). We have tried standard techniques of unsharp-masking as well as fitting and subtracting/dividing an elliptical surface brightness model in order to enhance the residual surface brightness structures. Unfortunately these techniques do not produce additional insight into the structure, likely due to the short exposure. Deeper X-ray data on A2443 are needed to search for additional cold fronts, better constrain the nature of the northern X-ray tail, and determine whether the tail has a clear signature of a sloshing spiral.

It is not clear what subhalo may be the perturber in the sloshing spiral scenario although we note that it is not unusual that the perturber is difficult to identify given the complexity of regions around clusters and the expected disruption of the perturber by the close encounter. Simulations of merger-induced sloshing by ZuHone et al. (2011) show that X-ray signatures persist for several Gyr following closest core passage. Assuming relative motion in the plane of the sky of 2000 km $s^{-1}$ between A2443 and ZwCl 2224.2+1651, the two systems would have had their closest approach roughly 1.3 Gyr ago, well within the timescale over which sloshing cores persist.

### 7.3. Surface Brightness Edges

In Section 5.3 we discuss the details of the two surface brightness edges we detect within A2443. As discussed above, the inner edge to the NE may be a cold front edge. Analysis of the temperature in large bins on either side of the edge shows cooler temperatures inside the edge and hotter temperatures outside. We note however that while the surface brightness profile shows a clear edge, we do not have sufficient counts to trace the temperature or pressure profiles in detail across the edge. Our model fits assume spherical symmetry, and we find a non-physical positive density slope inside the edge, therefore, future work on deeper X-ray data may require a more complex geometry to model the edge.

The outer edge to the SE is consistent with a shock, with inner temperatures higher than outer temperatures. The X-ray surface brightness has a best-fit density jump in the range of 1.2–1.8 (90% confidence). Although the density jump is consistent with a Mach number of $\mathcal{M} \approx 1.4$ shock, the measured temperature jump would imply a much stronger shock. Unfortunately, the temperature measurements had to be performed in very wide sectors on either side of the edge and are therefore not necessarily representative of the jump across the edge. In particular, with the current data we cannot distinguish a coarsely sampled temperature profile that smoothly drops with radius from a sharp jump across a shock edge. Deeper X-ray data will be required to trace the temperature on finer spatial scales. Confirmation of the merger shock would support the intermediate stage binary merger as we would not expect to detect a shock in a sloshing system that was driven only by a close encounter.

In principle the shock Mach number could be much higher than we estimate. If the shock is really a Mach 3–4 shock that we are viewing at an angle, then we would measure a much lower temperature and pressure jump due to projection effects. In addition, the density jump can also be underestimated for such a geometry if we are looking along a tangent to the Mach cone (i.e., the merger axis is not close to the plane of the sky).

### 7.4. Temperature Map

The X-ray temperature map in Figure 5 shows two hot regions located to the NE and SW of the cooler cluster core. We find that it is unlikely that these apparent hot regions could be driven by faint unresolved sources just below our *Chandra* detection limit.

One plausible interpretation for these two hot regions is that they are tracing the shock Mach cone which is being seen at some angle to the plane of the sky such that we are looking through the Mach cone. In this case, we would be seeing the cooler cluster core dominating the emission in the central region where the Mach cone is superimposed, and the hot regions of the Mach cone dominating in the outer, fainter regions on either side of the core. Unfortunately it would be very difficult to spectrally separate a cool cluster core component and hot shocked gas component even with very deep X-ray data.

### 7.5. Radio/X-Ray Connection

The spatial coincidence of the USS radio emission with the SE shock edge supports our interpretation of the radio emission as a radio relic. The elongated nature of the emission and non-central location are also typical of radio relics (Ferrari et al. 2008). The indication of a curved radio spectrum presented in Cohen & Clarke (2011) would suggest that the source may be an adiabatically compressed fossil radio lobe. DSA is able to produce USS relics but their spectrum would be expected to be power-law. Currently we only have flux measurement at three radio frequencies, thus we need to expand the radio frequency measurements to more clearly differentiate adiabatic compression from shock reacceleration of a pre-existing relativistic particle population. We note that in the shock reacceleration scenario, the low frequency integrated spectral index measured by CC11 of $\alpha_{74}^{325} = -1.7$ would be consistent with a $\mathcal{M} \approx 2.0$ shock which is plausible given our large uncertainties. We will explore the detailed spectral properties further in a future paper.

In the adiabatic compression model, the most likely candidate for the fossil plasma is the head-tail galaxy B. We have extracted the flux at 74 MHz and 330 MHz in three large, independent regions running from west to east along the length of the relic in order to estimate the variation of the spectral index along the source. We find that there is evidence of spectral steepening from west to east that is significant at the $7\sigma$ level. This steepening could be due to spectral aging of the relativistic plasma away from the head of source B. If the entire tail is active and/or revived plasma from source B, then we would be tracing the emission over a total arc length of 425 kpc from the head. We note, however, that the spectral variation we measure could also be produced by a variation in the Mach number along the shock edge, or by a spectral gradient in a pre-existing population of relativistic electrons that was reaccelerated by the shock passage.

Finally, we consider the possibility that the USS source may instead be a dying/dead radio galaxy. Integrated spectral measurements of dying radio galaxies show that they can be characterized by very steep, curved spectra (Murgia et al. 2011), similar to that of the A2443 USS source. We note, however, that the dying radio galaxies studied by Murgia et al. retain knowledge of their original spectrum such that spectral mapping shows the cores are flatter and the source steepens toward the

outer edges. In the case of the USS source in A2443, we see a spectral gradient with steepening from west to east rather than evidence of symmetric steepening from the center. This observed spectral signature does not appear to be consistent with the dying radio galaxy scenario. Deeper multi-frequency radio data will allow us to map the detailed spatial distribution of the spectral index and curvature and will help better distinguish these models.

## 8. SUMMARY

Our new *Chandra* observation shows the presence of a disturbed ICM in A2443 which is suggestive of a merging system. The ICM is elongated along a northwest to southeast direction, similar to the photometric cluster member distribution discussed by Wen et al. (2007). The central region of the cluster shows two X-ray edges which we tentatively identify as an inner cold front edge to the northeast of the core and an outer shock edge to the southeast of the core. There is also a cool X-ray tail seen to the north which may be ram pressure stripped material and/or a sloshing spiral. Based on the current data, we favor the model that the X-ray features are driven by an intermediate stage binary merger. The presence of multiple bright elliptical galaxies near the core supports the merger scenario.

The diffuse USS radio emission detected by CC11 is co-incident with the southeast shock edge; thus the non-central location and connection to a potential shock strengthens the identification of the emission as a radio relic. Based on the density jump at the southeast edge, we find that it is consistent with a Mach number $M \simeq 1.4$ shock, although the Mach number is still very uncertain due to the large uncertainties in the measurements. We interpret the two hot regions detected on either side of the central core as areas where we are viewing the Mach cone emission dominating the spectral fits while the cool core dominates in the center.

The steep spectral index and spectral curvature of the relic are suggestive of adiabatic compression of fossil radio plasma (possibly from the tail of radio galaxy B) as the origin of the relic. The size of the relic is slightly larger than expected for this model. With just a single high frequency flux measurement indicating spectral curvature, we do not rule out the possibility that the USS relic is due to shock reacceleration of fossil relativistic electrons. We have investigated the spatial distribution of the radio spectral index in three separate regions across the relic and find evidence of significant spectral steepening from the western edge to the eastern edge of the system. This spectral steepening would be consistent with what would be expected for spectral aging along the tail of source B.

T.E.C. was supported in part for this work by the National Aeronautics and Space Administration, through Chandra Award Number GO1-12007Z. Basic research in radio astronomy at the Naval Research Laboratory is supported by 6.1 Base funding. S.R. is supported by the Chandra X-ray Center through NASA contract NAS8-03060 and the Smithsonian Institution. C.L.S. was supported in part by NASA Chandra Grants GO9-0135X, GO9-0148X, and GO1-12169X, and NASA ADAP grant NNX11AD15G. E.L.B. was partially supported by NASA through the Astrophysics Data Analysis Program, grant number NNX10AC98G, and through NASA award RSA No. 1440385 issued by JPL/Caltech. S.G. acknowledges the support of NASA through Einstein Postdoctoral Fellowship PF0-110071 awarded by the Chandra X-ray Center. The National Radio Astronomy Observatory is a facility of the National Science Foundation operated under cooperative agreement by Associated Universities, Inc. This research has made use of the NASA/IPAC Extragalactic Database (NED) which is operated by the Jet Propulsion Laboratory, California Institute of Technology, under contract with the National Aeronautics and Space Administration.

Funding for SDSS-III has been provided by the Alfred P. Sloan Foundation, the Participating Institutions, the National Science Foundation, and the U.S. Department of Energy Office of Science. The SDSS-III Web site is http://www.sdss3.org/.

SDSS-III is managed by the Astrophysical Research Consortium for the Participating Institutions of the SDSS-III Collaboration including the University of Arizona, the Brazilian Participation Group, Brookhaven National Laboratory, University of Cambridge, Carnegie Mellon University, University of Florida, the French Participation Group, the German Participation Group, Harvard University, the Instituto de Astrofisica de Canarias, the Michigan State/Notre Dame/JINA Participation Group, Johns Hopkins University, Lawrence Berkeley National Laboratory, Max Planck Institute for Astrophysics, Max Planck Institute for Extraterrestrial Physics, New Mexico State University, New York University, Ohio State University, Pennsylvania State University, University of Portsmouth, Princeton University, the Spanish Participation Group, University of Tokyo, University of Utah, Vanderbilt University, University of Virginia, University of Washington, and Yale University.

We thank the anonymous referee for helpful comments.

## REFERENCES

Anders, E., & Grevesse, N. 1989, GeCoA, 53, 197
Ascasibar, Y., & Markevitch, M. 2006, ApJ, 650, 102
Blanton, E. L., Randall, S. W., Clarke, T. E., et al. 2011, ApJ, 737, 99
Bliton, M., Rizza, E., Burns, J. O., Owen, F. N., & Ledlow, M. J. 1998, MNRAS, 301, 609
Brandt, W. N., Alexander, D. M., Hornschemeier, A. E., et al. 2001, AJ, 122, 2810
Bourdin, H., Mazzotta, P., Markevitch, M., Giacintucci, S., & Brunetti, G. 2013, ApJ, 764, 82
Clarke, T. E., Blanton, E. L., & Sarazin, C. L. 2004, ApJ, 616, 178
Crawford, C. S., Allen, S. W., Ebeling, H., Edge, A. C., & Fabian, A. C. 1999, MNRAS, 306, 857
Cohen, A. S., & Clarke, T. E. 2011, AJ, 141, 149
Dennison, B. 1980, ApJL, 239, L93
Dickey, J. M., & Lockman, F. J. 1990, ARA&A, 28, 215
Diehl, S., & Statler, T. S. 2006, MNRAS, 368, 497
Enßlin, T. A., & Gopal-Krishna, 2001, A&A, 366, 26
Ensslin, T. A., Biermann, P. L., Klein, U., & Kohle, S. 1998, A&A, 332, 395
Feretti, L., Giovannini, G., Govoni, F., & Murgia, M. 2012, A&ARv, 20, 54
Ferrari, C., Govoni, F., Schindler, S., Bykov, A. M., & Rephaeli, Y. 2008, SSRv, 134, 93
Finoguenov, A., Sarazin, C. L., Nakazawa, K., Wik, D. R., & Clarke, T. E. 2010, ApJ, 715, 1143
Freeman, P. E., Kashyap, V., Rosner, R., & Lamb, D. Q. 2002, ApJS, 138, 185
Gutierrez, K., & Krawczynski, H. 2005, ApJ, 619, 161
Kale, R., & Dwarakanath, K. S. 2012, ApJ, 744, 46
Kang, H., & Ryu, D. 2011, ApJ, 734, 18
Kang, H., Ryu, D., & Jones, T. W. 2012, ApJ, 756, 97
Keshet, U. 2010, arXiv:1011.0729
Korngut, P. M., Dicker, S. R., Reese, E. D., et al. 2011, ApJ, 734, 10
Laganá, T. F., Andrade-Santos, F., & Lima Neto, G. B. 2010, A&A, 511, A15
Ma, C.-J., Owers, M., Nulsen, P. E. J., et al. 2012, ApJ, 752, 139
Macario, G., Markevitch, M., Giacintucci, S., et al. 2011, ApJ, 728, 82
Markevitch, M., Gonzalez, A. H., David, L., et al. 2002, ApJL, 567, L27
Markevitch, M., Govoni, F., Brunetti, G., & Jerius, D. 2005, ApJ, 627, 733
Markevitch, M., & Vikhlinin, A. 2007, PhR, 443, 1
Mazzotta, P., Bourdin, H., Giacintucci, S., Markevitch, M., & Venturi, T. 2011, MmSAI, 82, 495
Miller, C. J., Krughoff, K. S., Batuski, D. J., & Hill, J. M. 2002, AJ, 124, 1918
Murgia, M., Parma, P., Mack, K.-H., et al. 2011, A&A, 526, A148
Ogrean, G. A., Brüggen, M., van Weeren, R., et al. 2011, MNRAS, 414, 1175

Owers, M. S., Randall, S. W., Nulsen, P. E. J., et al. 2011, ApJ, 728, 27
Paterno-Mahler, R., Blanton, E. L., Randall, S. W., & Clarke, T. E. 2013, arXiv:1306.3520
Petrosian, V., & Bykov, A. M. 2008, SSRv, 134, 207
Pinzke, A., Oh, S. P., & Pfrommer, C. 2013, arXiv:1301.5644
Poole, G. B., Fardal, M. A., Babul, A., et al. 2006, MNRAS, 373, 881
Ptak, A., & Griffiths, R. 2003, in ASP Conf. Ser. 295, Astronomical Data Analysis Software and Systems XII, ed. H. E. Payne, R. I. Jedrzejewski, & R. N. Hook (San Francisco, CA: ASP), 465
Randall, S. W., Jones, C., Markevitch, M., et al. 2009, ApJ, 700, 1404
Randall, S., Nulsen, P., Forman, W. R., et al. 2008, ApJ, 688, 208
Russell, H. R., Sanders, J. S., Fabian, A. C., et al. 2010, MNRAS, 406, 1721
Sarazin, C. L. 2000, in IAP Meeting 2000, Constructing the Universe with Clusters of Galaxies, ed. F. Durret & D. Gerbal (Paris: IAP)
Simionescu, A., Werner, N., Urban, O., et al. 2012, ApJ, 757, 182
Slee, O. B., Roy, A. L., Murgia, M., Andernach, H., & Ehle, M. 2001, AJ, 122, 1172
Slee, O. B., Roy, A. L., & Savage, A. 1994, AuJPh, 47, 145
Struble, M. F., & Rood, H. J. 1999, ApJS, 125, 35
Truemper, J. 1993, Sci, 260, 1769
Trujillo, I., Aguerri, J. A. L., Gutiérrez, C. M., & Cepa, J. 2001, AJ, 122, 38
van Weeren, R. J., Intema, H. T., Oonk, J. B. R., Röttgering, H. J. A., & Clarke, T. E. 2009a, A&A, 508, 1269
van Weeren, R. J., Röttgering, H. J. A., & Brüggen, M. 2011, A&A, 527, A114
van Weeren, R. J., Röttgering, H. J. A., Brüggen, M., & Cohen, A. 2009b, A&A, 508, 75
Voges, W., Aschenbach, B., Boller, T., et al. 1999, A&A, 349, 389
Wen, Z.-L., Yang, Y.-B., Yuan, Q.-R., et al. 2007, ChJAA, 7, 71
Zacharias, N., Finch, C., Girard, T., et al. 2010, AJ, 139, 2184
ZuHone, J. A., Markevitch, M., Brunetti, G., & Giacintucci, S. 2013, ApJ, 762, 78
ZuHone, J. A., Markevitch, M., & Lee, D. 2011, ApJ, 743, 16